

Absence of Long-Range Magnetic Ordering in a Trirutile High-Entropy Oxide
(Mn_{0.2}Fe_{0.2}Co_{0.2}Ni_{0.2}Cu_{0.2})Ta₂O₆

Gina Angelo,^a Liana Klivansky,^b Jian Zhang,^b Xin Gui^{a}*

^a Department of Chemistry, University of Pittsburgh, Pittsburgh, PA, 15260, USA

^b The Molecular Foundry, Lawrence Berkeley National Laboratory, Berkeley, CA, 94720, USA

Abstract

Functionalities of solid-state materials are usually considered to be dependent on their crystal structures. The limited structural types observed in the emerged high-entropy oxides put constraints on exploration of their physical properties and potential applications. Herein, we synthesized the first high-entropy oxide in a trirutile structure, (Mn_{0.2}Fe_{0.2}Co_{0.2}Ni_{0.2}Cu_{0.2})Ta₂O₆, and investigated its magnetism. The phase purity and high-entropy nature were confirmed by powder X-ray diffraction and energy-dispersive spectroscopy, respectively. X-ray photoelectron spectroscopy indicated divalent Mn, Co and Cu along with coexistence of divalent and trivalent Fe and Ni. Magnetic properties measurements showed antiferromagnetic coupling and potential short-range magnetic ordering below ~ 4 K. The temperature-dependent heat capacity data measured under zero and high magnetic field confirmed the short-range magnetic ordering and a possible low-temperature phonon excitation. Moreover, the possible reasons for the absence of long-range magnetic ordering are concluded from a molecular orbital perspective. The discovery of the first trirutile high-entropy oxide opens a new way for studying the relationship between the highly disordered atomic arrangement and their magnetic interaction. Furthermore, it provides a new direction for exploring functionalities of high-entropy oxides.

Introduction

High-entropy oxides (HEOs) are a type of material where five or more elements are randomly distributed in equiatomic or near-equiatomic stoichiometry on the same atomic site. Vast applications such as catalysis¹ and reversible energy storage² were found for HEOs. Better mechanical properties and resistance to oxidation/corrosion were also observed for HEOs.^{3,4} In addition, magnetic insulating HEOs were reported due to their potential application in the next-generation memory and spintronic devices⁵. Since Rost et. al. discovered the first HEO in rocksalt structure⁶, there have been great efforts to expand the structural types of HEOs. To date, ten major crystal structures were found for HEOs: bixbyite (A_2O_3),⁷ delafossite (ABO_2),⁸ fluorite (AO_2),⁹ magnetoplumbite ($AB_{12}O_{19}$),¹⁰ mullite-type ($A_2B_4O_{10}$),¹¹ perovskite (ABO_3),¹² pyrochlore ($A_2B_2O_7$),^{13,14} rocksalt (AO),⁶ Ruddlesden-Popper phase ($A_{n+1}B_nO_{3n+1}$)¹⁵ and spinel (AB_2O_4)¹⁶ where A and B are cations. However, many structural types remain obscure, which significantly limits the manipulation and exploration of HEOs' properties. Furthermore, research surrounding their magnetic properties is only recently studied¹⁷. Upon investigation, HEOs can possess complicated magnetic properties due to the disordering of multiple transition metals, e.g., the spin-glass states in perovskite HEOs¹⁸ and tunable magnetism in spinel HEOs.¹⁶ Considering the importance of crystal structure in determining physical properties, expanding the structural families of HEOs is crucial for exploring their functionalities and potential applications.

Herein, we report the first trirutile HEO, $(Mn_{0.2}Fe_{0.2}Co_{0.2}Ni_{0.2}Cu_{0.2})Ta_2O_6$, belonging to space group $P 4_2/mnm$ (no. 136) evidenced by X-ray diffraction (XRD) and energy-dispersive spectroscopy (EDS). While there were reports of rutile HEOs¹⁹, the trirutile structure remains unfounded. Trirutile i.e. AB_2O_6 , is a derivative of the rutile structure i.e. AO_2 , wherein an additional element disrupts the repeatability of the rutile structure such that a $1 \times 1 \times 3$ superlattice is formed. We employed the trirutile compound $CoTa_2O_6$ as the parent compound, which was reported to be antiferromagnetically ordered below $T_N \sim 6.6$ K. However, when doped with Mg, i.e., $Co_{1-x}Mg_xTa_2O_6$, the antiferromagnetic ground state is quenched at $x=10\%$ while a short-range ferromagnetic correlation can be found in all series of compositions.²⁰ Considering that the theoretical calculations suggest the ferromagnetic ground state,²⁰ competing ferromagnetic and antiferromagnetic interactions must exist in $CoTa_2O_6$. Our investigation on the physical

properties of $(\text{Mn}_{0.2}\text{Fe}_{0.2}\text{Co}_{0.2}\text{Ni}_{0.2}\text{Cu}_{0.2})\text{Ta}_2\text{O}_6$ suggests short-range antiferromagnetic interaction resulting from the highly disordered transition-metal site. Therefore, the trirutile CoTa_2O_6 provides a good platform for investigating the interplay between magnetism and the crystallographic disorder on the Co site, with further possibilities to extend the scope of physical properties in trirutile HEOs.

Experimental Details

Synthesis of $(\text{Mn}_{0.2}\text{Fe}_{0.2}\text{Co}_{0.2}\text{Ni}_{0.2}\text{Cu}_{0.2})\text{Ta}_2\text{O}_6$

$(\text{Mn}_{0.2}\text{Fe}_{0.2}\text{Co}_{0.2}\text{Ni}_{0.2}\text{Cu}_{0.2})\text{Ta}_2\text{O}_6$ was prepared by mixing CoO powder (95%, Thermo Scientific), MnO powder (99.99%, Thermo Scientific), CuO powder (99.7%, -200 mesh, Alfa Aesar), NiO powder (99.998%, Thermo Scientific), Fe_2O_3 powder (99.9%, Thermo Scientific), and Ta_2O_5 powder (99.5% Thermo Scientific), and by placing the stoichiometric mixture into an alumina crucible. The crucible was heated to 1100 °C at a rate of 180 °C/hr, held overnight, then cooled at the same rate to room temperature. The sample was then thoroughly ground and mixed, pressed into a pellet, and heated to 1350 °C at a rate of 180 °C/hr. Subsequently, the sample was air quenched after being held at 1350 °C overnight. The resulting sample is a homogenous brown chunk and is stable in air.

Phase Identification:

$(\text{Mn}_{0.2}\text{Fe}_{0.2}\text{Co}_{0.2}\text{Ni}_{0.2}\text{Cu}_{0.2})\text{Ta}_2\text{O}_6$ was crushed into a powder and prepared for powder X-ray diffraction (XRD). A Bruker D2 PHASER was used with Cu K_α radiation ($\lambda = 1.54060 \text{ \AA}$, Ge monochromator). The Bragg angle measured was from 5 to 100 ° at a rate of 0.6 °/min with a step of 0.01 °. Rietveld fitting in FULLPROF was employed to analyze the crystal structure and test the phase purity of $(\text{Mn}_{0.2}\text{Fe}_{0.2}\text{Co}_{0.2}\text{Ni}_{0.2}\text{Cu}_{0.2})\text{Ta}_2\text{O}_6$.²¹

Physical Properties Measurements:

Magnetic Properties were measured in a Quantum Design Dynacool physical properties measurement system (PPMS) (1.8- 300 K, 0-9 T) equipped with AC Measurement System with both DC and AC magnetic fields available. Heat capacity was measured in the PPMS from 1.9 K to 37 K. Resistivity measurements were conducted in the PPMS from 310 K to 350 K using the four-probe method with platinum wires attached to the representative sample using silver epoxy.

Elemental Analysis:

Elemental analysis was performed via scanning electron microscopy (SEM) with energy-dispersive spectroscopy (EDS). A Zeiss Sigma 500 VP SEM with Oxford Aztec X-EDS was used with an electron beam energy of 20 kV.

Oxidation States Analysis:

X-ray photoelectron spectroscopy (XPS) was performed in a Thermo Scientific™ K-AlphaPlus™ instrument equipped with monochromatic Al K α radiation (1486.7 eV) as the excitation source. The X-ray analysis area for measurement was set at 200 x 400 μ m (ellipse shape) and a flood gun was used for charge compensation. The pass energy was 200 eV for the wide (survey) spectra and 50 eV for the high-resolution regions (narrow spectra). The base pressure of the analysis chamber was less than $\sim 1 \times 10^{-9}$ mbar. The analysis chamber pressure was at 1×10^{-7} mbar during data acquisition. Data were collected and processed using the Thermo Scientific Advantage XPS software package.

Results and Discussion

Crystal structure and elemental analysis: Powder XRD pattern of the air-quenched sample from 5 to 100 ° is shown in Figure 1(c). The pattern was fitted via Rietveld method by using the crystal structure of reported CoTa₂O₆.²² The fitting parameters, i.e., $R_p=3.30$, $R_{wp} = 4.36$, $R_{exp} = 2.44$ and $\chi^2 = 3.21$, showed good match between the trirutile CoTa₂O₆ and the proposed HEO (Mn_{0.2}Fe_{0.2}Co_{0.2}Ni_{0.2}Cu_{0.2})Ta₂O₆. No secondary phase except for trace amount of Ta₂O₅ was found, indicating that (Mn_{0.2}Fe_{0.2}Co_{0.2}Ni_{0.2}Cu_{0.2})Ta₂O₆ crystallizes in the same space group as CoTa₂O₆, i.e., $P 4_2/mnm$. The minor impurity of Ta₂O₅ may be resulted from vaporization of CuO due to its low melting point (~ 1325 °C). The refined lattice parameters of (Mn_{0.2}Fe_{0.2}Co_{0.2}Ni_{0.2}Cu_{0.2})Ta₂O₆ are $a = 4.73483(3)$ Å , $c = 9.19965(5)$ Å , which creates a slightly larger unit cell than the low-entropy parent compound CoTa₂O₆ ($a = 4.73580$ Å , $c = 9.17080$ Å) with larger tetragonality, i.e., larger c/a ratio. The fitted atomic coordinates are shown in Table S1 in the supporting information, which further confirms the trirutile structure for (Mn_{0.2}Fe_{0.2}Co_{0.2}Ni_{0.2}Cu_{0.2})Ta₂O₆. The obtained crystal structure is shown in Figures 1(a) & 1(b). Edge-shared M@O₆ and Ta@O₆ octahedra stack along the c axis and are connected with each other in a corner-sharing manner. The M@O₆ layers with high-entropy site consisting of 3d transition metals within ab plane are separated by Ta@O₆ layers.

In order to confirm the high-entropy nature of (Mn_{0.2}Fe_{0.2}Co_{0.2}Ni_{0.2}Cu_{0.2})Ta₂O₆, SEM-EDS analysis was performed. In three distinct regions of (Mn_{0.2}Fe_{0.2}Co_{0.2}Ni_{0.2}Cu_{0.2})Ta₂O₆, elemental maps can be seen in Figure 1(d), and four points were tested for which the results are shown in Table S2 in the supporting information. The average chemical formula was found to be

$\text{Mn}_{0.19(2)}\text{Fe}_{0.26(6)}\text{Co}_{0.21(2)}\text{Ni}_{0.25(11)}\text{Cu}_{0.19(4)}\text{Ta}_{2.0(1)}\text{O}_6$, within the error of loading composition, and all subsequent calculations were performed based on this formula.

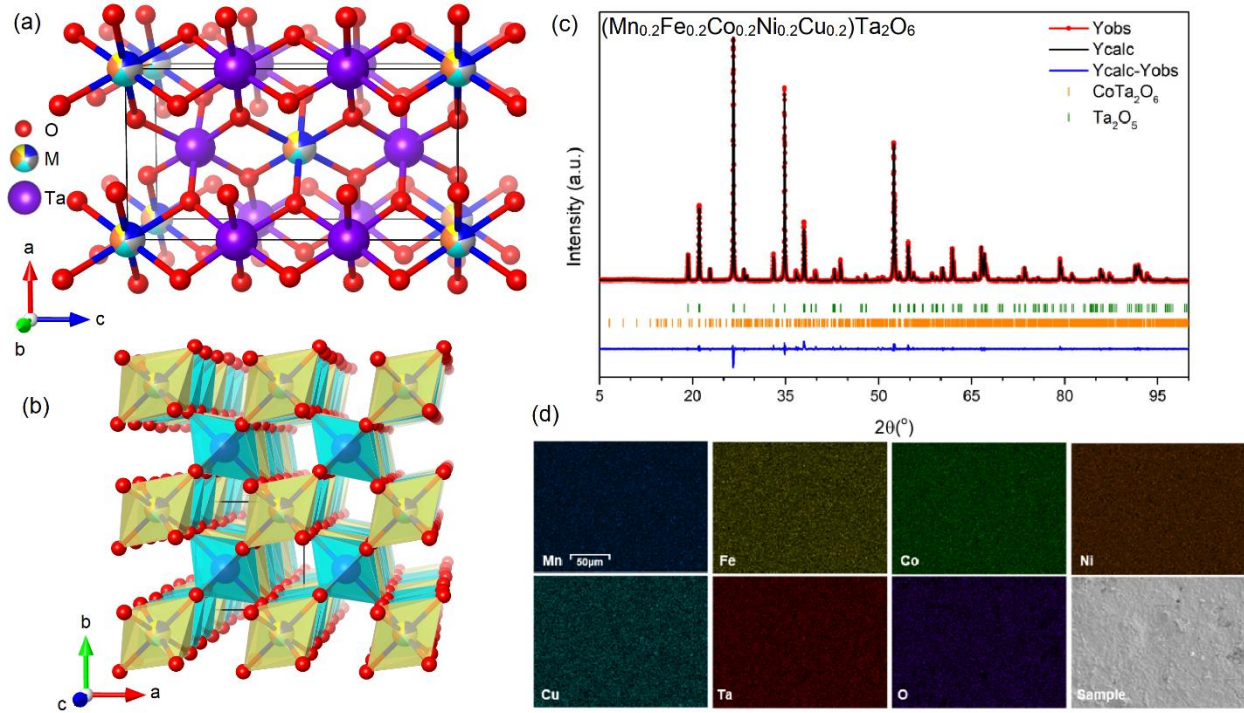


Figure 1 (a) $(\text{Mn}_{0.2}\text{Fe}_{0.2}\text{Co}_{0.2}\text{Ni}_{0.2}\text{Cu}_{0.2})\text{Ta}_2\text{O}_6$ trirutile structure viewing from the b axis and (b) $(\text{Mn}_{0.2}\text{Fe}_{0.2}\text{Co}_{0.2}\text{Ni}_{0.2}\text{Cu}_{0.2})\text{Ta}_2\text{O}_6$ viewing from the c axis with Ta@O_6 (cyan) and M@O_6 (yellow) octahedra. Here, “M” stands for the $3d$ transition metals in $(\text{Mn}_{0.2}\text{Fe}_{0.2}\text{Co}_{0.2}\text{Ni}_{0.2}\text{Cu}_{0.2})\text{Ta}_2\text{O}_6$. (c) Powder XRD pattern of $(\text{Mn}_{0.2}\text{Fe}_{0.2}\text{Co}_{0.2}\text{Ni}_{0.2}\text{Cu}_{0.2})\text{Ta}_2\text{O}_6$. The observed pattern is shown by the red line with dots while the black line represents the calculated pattern. The difference between the observed and calculated pattern is shown in blue. Bragg peaks positions of $(\text{Mn}_{0.2}\text{Fe}_{0.2}\text{Co}_{0.2}\text{Ni}_{0.2}\text{Cu}_{0.2})\text{Ta}_2\text{O}_6$ and Ta_2O_5 are visualized with green and orange vertical bars, respectively. (d) SEM-EDS elemental mapping results of Co, Cu, Fe, Mn, Ni, Ta, and O on a 200- μm area of an annealed pellet.

Short-range antiferromagnetic ordering in $(\text{Mn}_{0.2}\text{Fe}_{0.2}\text{Co}_{0.2}\text{Ni}_{0.2}\text{Cu}_{0.2})\text{Ta}_2\text{O}_6$:

$(\text{Mn}_{0.2}\text{Fe}_{0.2}\text{Co}_{0.2}\text{Ni}_{0.2}\text{Cu}_{0.2})\text{Ta}_2\text{O}_6$ was measured for the temperature dependence of magnetic susceptibility from 1.8 to 300 K under an external magnetic field of 0.1 T in a zero-field cooling mode, as shown in Figure 2(a). Paramagnetic behavior was seen above ~ 75 K while a broad peak can be observed at ~ 4 K, as discussed later. The χ^{-1} vs T curve is mainly linear, only deviating at high temperatures above ~ 250 K due to instrumental sensitivity and low temperatures below ~ 50 K, as discussed later. Curie-Weiss (CW) fitting was performed from 75 to 250 K according to the CW law:

$$\chi = \frac{C}{T - \theta_{CW}}$$

where χ is the magnetic susceptibility, C is a constant independent of temperature and related to the effective moment (μ_{eff}), and θ_{CW} is the CW temperature. The resulted θ_{CW} is -14.07 (1) K, indicating antiferromagnetic (AFM) spin-spin coupling within the fitted temperature region. Therefore, the slight deviation from CW behavior below ~ 40 K might originate from the onset of AFM coupling, as seen in Figure S1 in the supporting information.

Based on $\mu_{eff} \text{ (spin-only)} = \sqrt{n(n+2)}$ where n is the number of unpaired electrons, the spin-only moment for all 3d transition metal ions in high-spin octahedral crystal field in our material are as follows: Mn^{2+} ($\sim 5.92 \mu_B$), Fe^{2+} ($\sim 4.89 \mu_B$), Fe^{3+} ($\sim 5.92 \mu_B$), Co^{2+} ($\sim 3.88 \mu_B$), Ni^{2+} ($\sim 2.83 \mu_B$), Ni^{3+} ($\sim 3.88 \mu_B$) and Cu^{2+} ($\sim 1.73 \mu_B$). Two oxidation states of Fe are considered here due to the usage of Fe_2O_3 as starting material while the divalent nature of the Co^{2+} site in $CoTa_2O_6$. Ni^{3+} is taken into account due to XPS results and observed short-range magnetic ordering, as described later. When considering only Fe^{2+} and Ni^{2+} (that is without Fe^{3+} and Ni^{3+}), μ_{eff} averages to $\sim 3.85 \mu_B/\text{f.u.}$ When considering only Fe^{3+} and Ni^{3+} (without Fe^{2+} and Ni^{2+}), the average is $\sim 4.27 \mu_B/\text{f.u.}$ The μ_{eff} from CW fitting was determined via $\mu_{eff} = \sqrt{8C}$ to

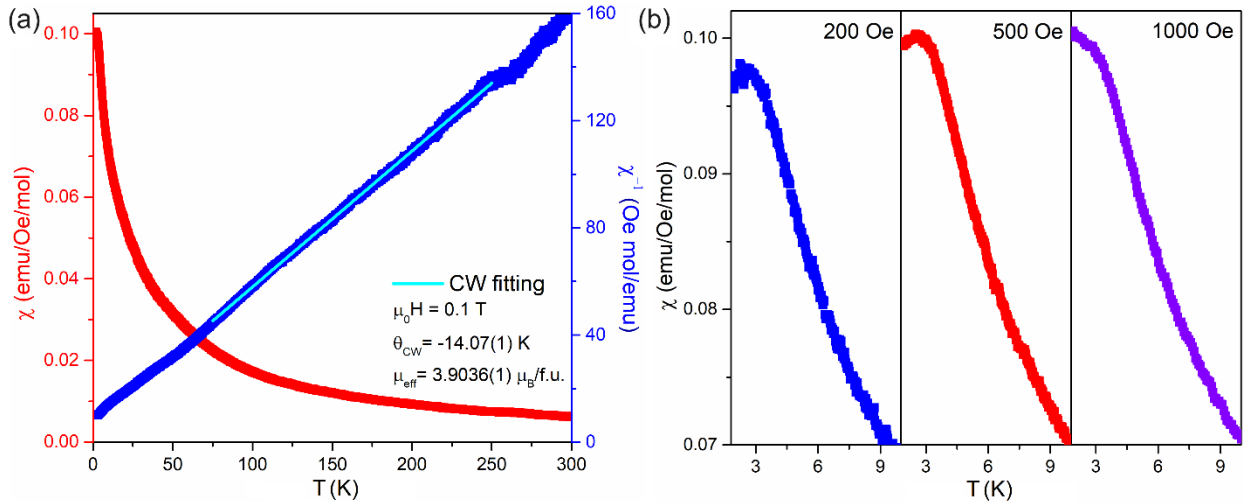


Figure 2 (a) Magnetic susceptibility (left red axis) and inverse of magnetic susceptibility (right blue axis) of $(Mn_{0.2}Fe_{0.2}Co_{0.2}Ni_{0.2}Cu_{0.2})Ta_2O_6$ measured under an external magnetic field of 0.1 T with respect to temperature. The cyan line represents the Curie-Weiss fitting. (b) Magnetic susceptibility of $(Mn_{0.2}Fe_{0.2}Co_{0.2}Ni_{0.2}Cu_{0.2})Ta_2O_6$ from 1.8 to 10K under 200, 500, and 1000 Oe depicted in blue, red, and violet curves, respectively.

be $3.9036(1) \mu_B/\text{f.u.}$, implying that Fe and Ni are likely divalent in this material while a portion of Fe^{3+} and Ni^{3+} may also exist, which is further evidenced by XPS data shown later.

As shown in Figure 2(b), the χ vs T curve goes from downward parabola shape below ~ 4 K to more linear shape at low temperatures with increasing magnetic field, probably due to the increasing spin polarization of local magnetic moments on 3d transition metal cations. Therefore, under low field, short range antiferromagnetic interactions exist and that leads to the broad peak; however, the feature disappears with increasing field since the ions are immediately polarized. AC magnetic susceptibility was also measured under 1000 Hz, 3000 Hz and 4000 Hz from 2 K to 16 K, as seen in Figure S2 in the supporting information, with the applied DC magnetic field of 100 Oe. The same broad peak can be observed under ~ 4 K as Figure 2(b), however, no shift of the peak position was seen. Such a behavior excludes the possibility of spin-glass state in $(\text{Mn}_{0.2}\text{Fe}_{0.2}\text{Co}_{0.2}\text{Ni}_{0.2}\text{Cu}_{0.2})\text{Ta}_2\text{O}_6$.

The field-dependence of magnetization, as shown in Figure 3, illustrates that at 2, 10, and 300 K, $(\text{Mn}_{0.2}\text{Fe}_{0.2}\text{Co}_{0.2}\text{Ni}_{0.2}\text{Cu}_{0.2})\text{Ta}_2\text{O}_6$ does not become saturated from up to 9 T. A slightly bent feature can be seen under 2 K, which is typical for paramagnetic state or the scenario with short-range magnetic ordering. In addition, no coercive field is observed, as can be seen in Figure S3 in the supporting information, which can be the indicative of the absence of a long-range ordered ferromagnetic component.

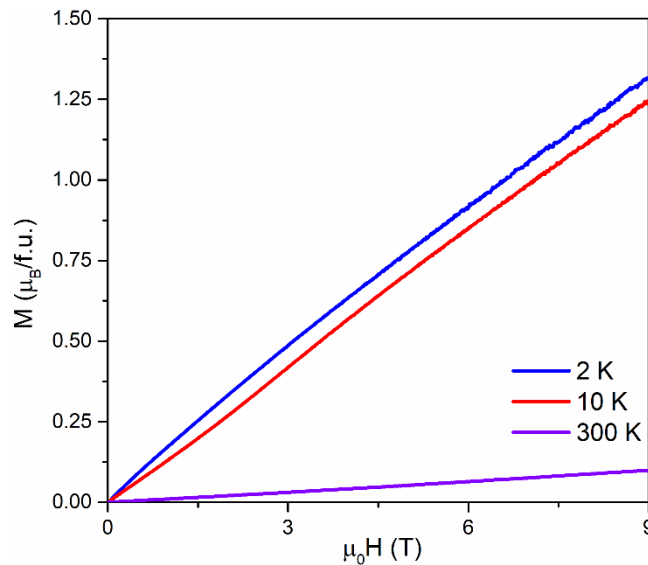


Figure 3. Field-dependent magnetization of $(\text{Mn}_{0.2}\text{Fe}_{0.2}\text{Co}_{0.2}\text{Ni}_{0.2}\text{Cu}_{0.2})\text{Ta}_2\text{O}_6$ from 0-9 T at 2, 10, and 300 K in blue, red, and violet, respectively.

Heat Capacity: The temperature-dependent heat capacity of $(\text{Mn}_{0.2}\text{Fe}_{0.2}\text{Co}_{0.2}\text{Ni}_{0.2}\text{Cu}_{0.2})\text{Ta}_2\text{O}_6$ was measured from 1.9 to ~ 37 K. No indication of long-range magnetic ordering, i.e., a peak in heat capacity curve, can be seen, as shown in Figure 4(a). While a kink appears at ~ 5 K in Figure 4(a), Figure 4(b) plots the C_{total}/T vs T curve and a peak is shown at ~ 5 K. The total heat capacity of a magnetic material can be treated as the sum of electronic, phononic, and magnonic contribution where $C_{\text{total}} = C_{\text{el}} + C_{\text{ph}} + C_{\text{mag}}$. As shown by resistivity in Figure S4 in the supporting information, $(\text{Mn}_{0.2}\text{Fe}_{0.2}\text{Co}_{0.2}\text{Ni}_{0.2}\text{Cu}_{0.2})\text{Ta}_2\text{O}_6$ is an insulator, thus there are no electronic contributions to heat capacity, i.e., $C_{\text{total}} = C_{\text{ph}} + C_{\text{mag}}$. As an estimate, $C_{\text{ph}} = \beta T^3$ according to the Debye formula where β is the vibrational contribution coefficient. However, just a T^3 term could not lead to a good fitting. Herein, T^5 , T^7 , T^9 , and T^{11} terms were added to obtain a reasonable fitting so that a polynomial fit was employed: $C_{\text{ph}}/T = \beta_1 T^2 + \beta_2 T^4 + \beta_3 T^6 + \beta_4 T^8 + \beta_5 T^{10}$ where β_1 , β_2 , β_3 , β_4 , and β_5 are constants and were fitted to $0.00240(3)$ J/mol/K⁴, $-5.5(1) \times 10^{-6}$ J/mol/K⁶, $6.3(2) \times 10^{-9}$ J/mol/K⁸, $-3.5(2) \times 10^{-12}$ J/mol/K¹⁰, and $7.5(4) \times 10^{-16}$ J/mol/K¹². Therefore, by subtracting the phononic contribution from C_{total}/T , pure C_{mag}/T is plotted in Figure 4(b) as blue open circles. By integrating C_{mag}/T vs T curve, the change in magnetic entropy, ΔS_{mag} , is obtained. ΔS_{mag} is usually determined by the spin multiplicity in a magnetic system where contributions from orbital angular momentum can be ignored by $\Delta S_{\text{mag}} = R \ln(2S+1)$ where R is the gas constant. Here, ΔS_{mag} does not exceed $R \ln 2$, which is the magnetic entropy

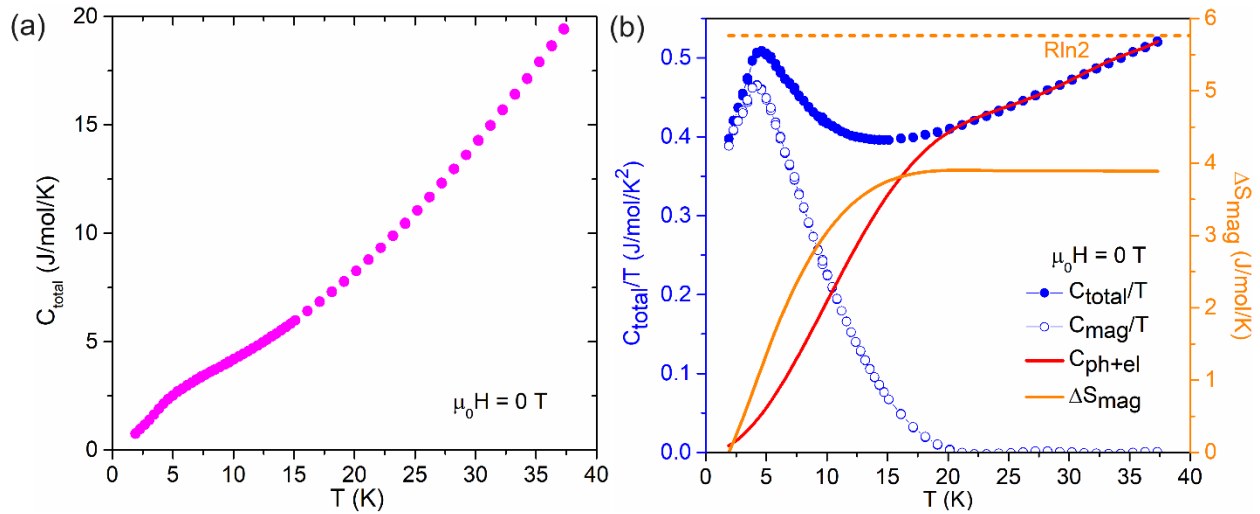


Figure 4 (a). C_{total} is shown in magenta as a function of temperature. **(b)** C_{total}/T is shown in blue filled circles while C_{mag}/T is shown in blue open circles. The fitted C_{ph} is graphed in red. These three curves correspond to the left blue axis. $R \ln 2$ is shown by the orange dashed line and ΔS_{mag} is the solid orange line; both lines correspond to the right orange axis.

change for a $S = 1/2$ system. Because the average spin state of the 3d transition metals appearing in $(\text{Mn}_{0.2}\text{Fe}_{0.2}\text{Co}_{0.2}\text{Ni}_{0.2}\text{Cu}_{0.2})\text{Ta}_2\text{O}_6$, i.e., Mn^{2+} ($S = 5/2$), Fe^{2+} ($S = 2$), Fe^{3+} ($S = 5/2$), Co^{2+} ($S = 3/2$), Ni^{2+} ($S = 1$), Ni^{3+} ($S = 3/2$) and Cu^{2+} ($S = 1/2$), must be larger than $S = 3/2$, that is, the total spin angular momentum when only divalent species are considered. Therefore, the observed ΔS_{mag} is obviously smaller than $R\ln 4$, indicating the absence of long-range magnetic ordering within the measured temperature range in $(\text{Mn}_{0.2}\text{Fe}_{0.2}\text{Co}_{0.2}\text{Ni}_{0.2}\text{Cu}_{0.2})\text{Ta}_2\text{O}_6$. Heat capacity of $(\text{Mn}_{0.2}\text{Fe}_{0.2}\text{Co}_{0.2}\text{Ni}_{0.2}\text{Cu}_{0.2})\text{Ta}_2\text{O}_6$ was also measured under an external magnetic field, as shown in Figure S5 in the supporting information. A slight decrease in peak intensity is seen while no shift is observed for peak position. The field-independent behavior suggests that such anomaly below ~ 5 K may consist of two parts, the short-range magnetic ordering as described in the magnetic properties, and the phononic excitation at ~ 4 K that is not affected by external magnetic field. Therefore, the decrease in peak intensity can be resulted from the suppression of short-range magnetic ordering under high external magnetic field, i.e., the polarization of magnetic dipole moments under magnetic field.

Oxidation states of transition metal ions: XPS results shown in Figures 5(a) -5(e) highlight the 2p orbitals of each 3d transition metal ions. Observed (expected) spin orbital splitting are as follows: Mn, 11.3 eV (11.2 eV), Fe (II) 13.7 eV (13 eV), Fe (III) 13.5 eV (13 eV), Co 15.3 eV (14.99 eV), Ni (II) 16.9 eV (17.3 eV), Ni (III) 16.9 eV (17.3 eV), and Cu 19.8 eV (19.75 eV). Satellite peaks present in all spectra but Ni, consistent with other reports.²³ Fe clearly has two sets of peaks at 711.6 eV and 725.3 eV ($2p_{3/2}$ and $2p_{1/2}$) and 714.0 eV and 727.5 eV ($2p_{3/2}$ and $2p_{1/2}$), corresponding to two different oxidation states, i.e., Fe^{2+} and Fe^{3+} . Ni also has two sets of peaks at 855.2 eV and 872.1 eV ($2p_{3/2}$ and $2p_{1/2}$) and 861.8 eV and 878.7 eV ($2p_{3/2}$ and $2p_{1/2}$), corresponding to two different oxidation states, i.e., Ni^{2+} and Ni^{3+} . The XPS results on the coexistence of $\text{Fe}^{2+}/\text{Fe}^{3+}$ and $\text{Ni}^{2+}/\text{Ni}^{3+}$ are consistent with magnetic data described above. The peak positions are also comparable to what were reported in the literature for octahedral $\text{Fe}^{2+}/\text{Fe}^{3+}$ and $\text{Ni}^{2+}/\text{Ni}^{3+}$.^{23,24} Only one set of peaks for $2p_{3/2}$ and $2p_{1/2}$ were fitted for other transition metals, without a clear distinction of more than one oxidation state. For Co, the peaks corresponding to $2p_{3/2}$ and $2p_{1/2}$ are at 781.6 eV and 796.9 eV, which are consistent with reported Co^{2+} .²³ Similarly, the $2p_{3/2}$ and $2p_{1/2}$ peaks in the Mn (643.1 and 654.4 eV) and Cu (933.7 and 953.5 eV) spectra are consistent with Mn^{2+} ,²³ and Cu^{2+} .²⁵ Therefore, the XPS results confirmed the spin states that we speculated from the magnetic data.

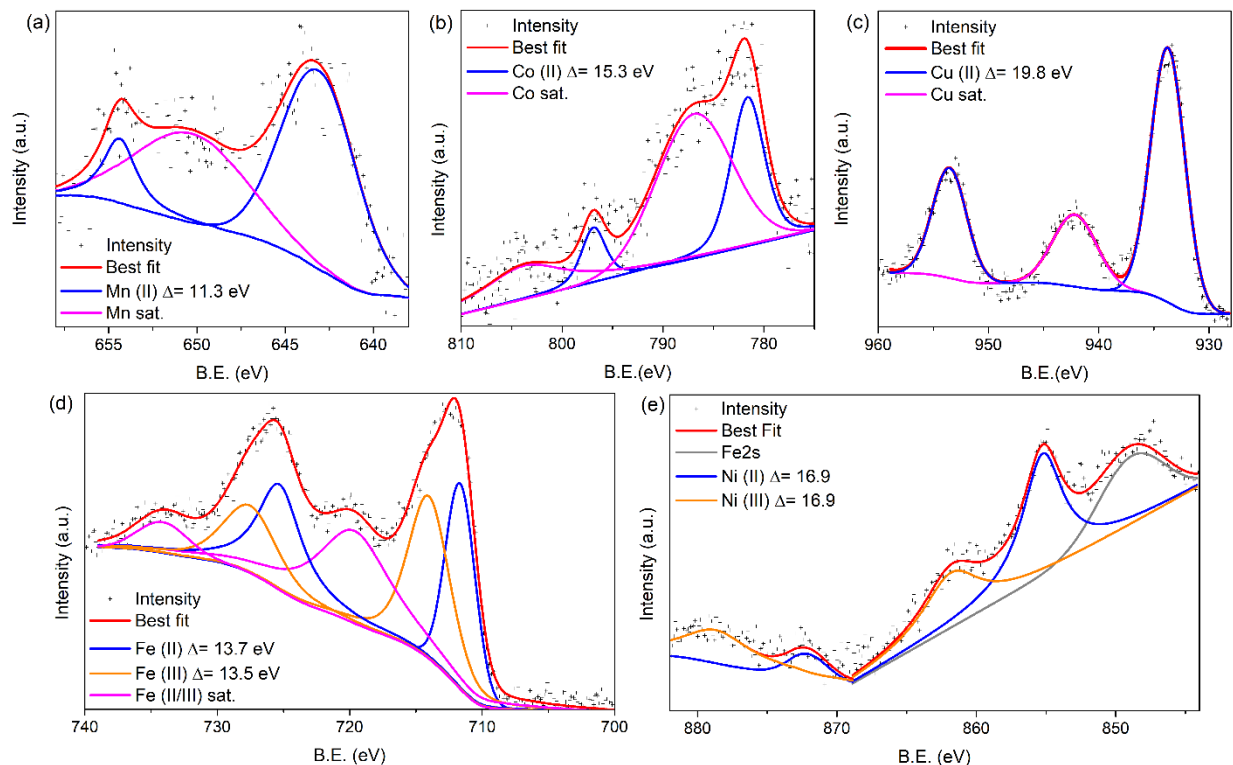


Figure 5. XPS of $(\text{Mn}_{0.2}\text{Fe}_{0.2}\text{Co}_{0.2}\text{Ni}_{0.2}\text{Cu}_{0.2})\text{Ta}_2\text{O}_6$ in range of $2p$ orbitals for (a) Mn, (b) Co, (c) Cu, (d) Fe and (e) Ni. In each graph, the line of best fit is shown in red. Pairs of peaks are shown in coordinating colors (blue and orange) while satellite peaks are shown in magenta. The grey curve in (e) depicts Fe $2s$ in the Ni $2p$ range. B.E. stands for binding energy.

Magnetic superexchange interaction and possible origin of short-range magnetic ordering:

Based on the crystal structure of $(\text{Mn}_{0.2}\text{Fe}_{0.2}\text{Co}_{0.2}\text{Ni}_{0.2}\text{Cu}_{0.2})\text{Ta}_2\text{O}_6$, two possible magnetic superexchange pathways can be proposed, as illustrated in Figure 6, while the other pathways are related with them by symmetries. The atomic orbitals of $\text{M}^{2+/3+}$ near the Fermi energy are determined by the Semi-empirical extended-Hückel-tight-binding (EHTB) methods and CAESAR packages, as described in the supporting information. The calculation was only conducted on the parent compound, CoTa_2O_6 , due to the complexities of the high-entropy $(\text{Mn}_{0.2}\text{Fe}_{0.2}\text{Co}_{0.2}\text{Ni}_{0.2}\text{Cu}_{0.2})\text{Ta}_2\text{O}_6$. However, the symmetries of molecular orbitals in CoTa_2O_6 can be well extended to $(\text{Mn}_{0.2}\text{Fe}_{0.2}\text{Co}_{0.2}\text{Ni}_{0.2}\text{Cu}_{0.2})\text{Ta}_2\text{O}_6$ regardless of addition or removal of valence electrons of $3d$ transition metal ions. Therefore, the analysis of molecular orbitals in the high-entropy compound can be conducted based on the highest-occupied molecular orbital in CoTa_2O_6 by varying the number of electrons.

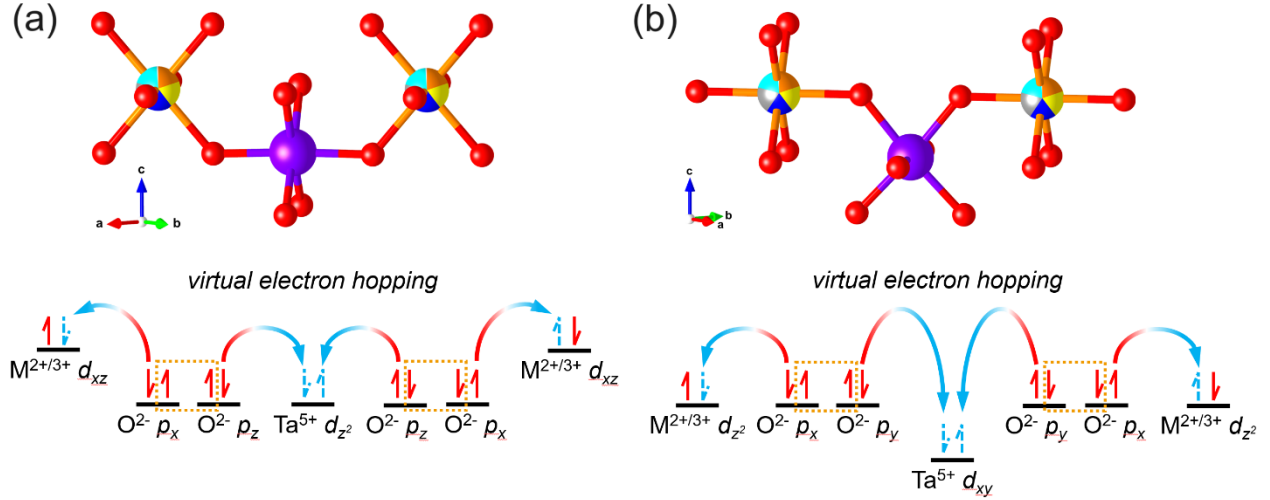


Figure 6. The two different magnetic superexchange pathways in $(\text{Mn}_{0.2}\text{Fe}_{0.2}\text{Co}_{0.2}\text{Ni}_{0.2}\text{Cu}_{0.2})\text{Ta}_2\text{O}_6$ between transition metal ions. $\text{M}^{2+/3+}$ stand for transition metal ions. The relative vertical distance between atomic orbitals stands for the relative geometry of ions. The dashed orange lines involve the pair of electrons on difference p orbitals of oxygen ions that stabilize the superexchange pathways by inclusion of exchange energy.

The first superexchange pathway is shown in Figure 6(a) where two M@O_6 octahedra are connected by Ta@O_6 octahedron via an axial manner. In this case, half-filled d_{xz} orbital of $\text{M}^{2+/3+}$, fully-filled p_x and p_z orbitals of O^{2-} and empty d_z^2 orbital of Ta^{5+} are present. The two $\text{M}^{2+/3+}$ ions on the opposite sides show antiferromagnetic coupling due to the following reasons: 1. due to the virtual electron hopping represented by the arrows, a pair of spins with opposite spin directions from oxygen p_z orbitals can populate the empty d_z^2 orbital of Ta^{5+} , which provides a more stable ground state; 2. the exchange energies between the spins with the same direction on p_x and p_z orbitals of O^{2-} stabilize the system as well, as indicated by the orange dashed lines in Figure 6; 3. virtual electron hopping can also occur between the p_x orbitals of O^{2-} and the half-filled d_{xz} orbital of $\text{M}^{2+/3+}$, which leads to a stable singlet state. The superexchange interaction depicted above results in the antiferromagnetic coupling between the $\text{M}^{2+/3+}$ ions. Similar reasons and superexchange pattern can be found in the second pathway, shown in Figure 6(b), while the involved atomic orbitals are now the half-filled d_z^2 orbital of $\text{M}^{2+/3+}$, fully-filled p_x and p_y orbitals of O^{2-} and empty d_{xy} orbital of Ta^{5+} . In both cases, antiferromagnetic coupling between M ions is dominant.

With the analysis above, we can speculate three possible reasons of the short-range magnetic ordering observed in magnetic properties measurements:

- The existence of Ni^{2+} and Cu^{2+} leads to the lack of half-filled d_{xz} orbitals, which disables the scenario in Figure 6(a) where a half-filled d_{xz} orbital of $\text{M}^{2+/3+}$ is necessary. Subsequently, the corresponding superexchange pathway is not functional due to the lack of electron hopping and, thus, magnetic coupling is absent. Meanwhile, all the $\text{M}^{2+/3+}$ ions possess a half-filled d_z^2 orbital, which allows the superexchange interaction in Figure 6(b). Therefore, with part of the superexchange pathways disabled, long-range magnetic ordering does not exist in $(\text{Mn}_{0.2}\text{Fe}_{0.2}\text{Co}_{0.2}\text{Ni}_{0.2}\text{Cu}_{0.2})\text{Ta}_2\text{O}_6$.
- Due to the existence of Fe^{3+} and Ni^{3+} , in order to maintain charge balance, possible removal of cations can take place as a result of ionic charge compensation mechanism. Therefore, part of the M^{2+} or Ta^{5+} sites may be vacant, leading to the interruption of the superexchange pathways and the absence of long-range magnetic ordering.
- The high-entropy nature of the $\text{M}^{2+/3+}$ site can result in the local distortion of the M@O_6 octahedra, which reduces the orbital overlap between $\text{M}^{2+/3+}$ and the intermediate O^{2-} . Consequently, electron hopping may not occur due to the altered symmetries of orbitals.

Conclusion

In this paper, we reported the first high-entropy oxide in a trirutile structure. High-purity phase with high configurational disorder in a uniform structure has been determined via powder XRD and EDS measurements. The new material, $(\text{Mn}_{0.2}\text{Fe}_{0.2}\text{Co}_{0.2}\text{Ni}_{0.2}\text{Cu}_{0.2})\text{Ta}_2\text{O}_6$, shows antiferromagnetic spin-spin coupling under high temperatures while exhibiting short-range antiferromagnetic ordering under low temperatures. Heat capacity further shows the evidence of the absence of long-range magnetic ordering in this compound. XPS shows the presence of both Fe^{2+} and Fe^{3+} as well as Ni^{2+} and Ni^{3+} along with divalent Mn, Co and Cu, which are consistent with the observation in the magnetic results. The discovery of the first trirutile high-entropy oxide builds a new platform for investigating the interplay between high-entropy nature and their magnetism. Moreover, it allows the manipulation of a wider range of physical properties in high-entropy oxides.

Associated Content

Supporting Information

The Supporting Information is available free of charge at XXX.

Deviation from Curie-Weiss behavior below ~50 K. AC magnetic susceptibility data. Magnetic hysteresis loop. Temperature-dependent resistivity data. Heat capacity data under zero and applied magnetic field. Powder XRD fitted atomic coordinates. EDS results.

Author Information

Corresponding Author: xig75@pitt.edu

Notes: The authors declare no competing financial interest.

Acknowledgements

G. A. and X.G. are supported by the startup fund from the University of Pittsburgh and the Pitt Momentum Fund. Portions of this work were performed at the Molecular Foundry and supported by the Office of Science, Office of Basic Energy Sciences, of the U.S. Department of Energy under Contract No. DE-AC02-05CH11231.

References

- (1) Feng, D.; Dong, Y.; Zhang, L.; Ge, X.; Zhang, W.; Dai, S.; Qiao, Z. Holey Lamellar High-Entropy Oxide as an Ultra-High-Activity Heterogeneous Catalyst for Solvent-free Aerobic Oxidation of Benzyl Alcohol. *Angew. Chem. Int. Ed.* **2020**, *132*, 19671–19677. <https://doi.org/10.1002/ange.202004892>.
- (2) Sarkar, A.; Velasco, L.; Wang, D.; Wang, Q.; Talasila, G.; De Biasi, L.; Kübel, C.; Brezesinski, T.; Bhattacharya, S. S.; Hahn, H.; Breitung, B. High Entropy Oxides for Reversible Energy Storage. *Nat. Comm.* **2018**, *9*, 3400. <https://doi.org/10.1038/s41467-018-05774-5>.
- (3) Tyagi, P. K.; Jha, S. K. Flash Sintering Improves the Densification and Mechanical Properties of High Entropy Oxides Used in Anodic Applications. *Materialia* **2024**, *33*, 101967. <https://doi.org/10.1016/j.mtla.2023.101967>.
- (4) Ujah, C. O.; Kallon, D. V. V.; Aigbodion, V. S. Corrosion Characteristics of High-Entropy Alloys Prepared by Spark Plasma Sintering. *Int. J. Adv. Manuf. Technol.* **2024**, *132*, 63–82. <https://doi.org/10.1007/s00170-024-13452-8>.
- (5) Sharma, Y.; Mazza, A. R.; Musico, B. L.; Skoropata, E.; Nepal, R.; Jin, R.; Ievlev, A. V.; Collins, L.; Gai, Z.; Chen, A.; Brahlek, M.; Keppens, V.; Ward, T. Z. Magnetic Texture in Insulating Single Crystal High Entropy Oxide Spinel Films. *ACS Appl. Mater. Interfaces* **2021**, *13*, 17971–17977. <https://doi.org/10.1021/acsami.1c01344>.
- (6) Rost, C. M.; Sachet, E.; Borman, T.; Moballegh, A.; Dickey, E. C.; Hou, D.; Jones, J. L.; Curtarolo, S.; Maria, J.-P. Entropy-Stabilized Oxides. *Nat. Comm.* **2015**, *6*, 8485. <https://doi.org/10.1038/ncomms9485>.
- (7) Park, T.; Javadinejad, H. R.; Kim, Y.-K.; Chang, H. J.; Choi, H.; Woong, C.; Ashong, A. N.; Lee, Y. S.; Kim, J. H. Effect of Processing Route on the Crystal Structure and Physical Properties of Bixbyite High-Entropy Oxides. *J. Alloys Compd.* **2022**, *893*, 162108. <https://doi.org/10.1016/j.jallcom.2021.162108>.
- (8) Wang, J.; Cui, Y.; Wang, Q.; Wang, K.; Huang, X.; Stenzel, D.; Sarkar, A.; Azmi, R.; Bergfeldt, T.; Bhattacharya, S. S.; Kruk, R.; Hahn, H.; Schweidler, S.; Brezesinski, T.; Breitung, B. Lithium Containing Layered High Entropy Oxide Structures. *Sci. Rep.* **2020**, *10*, 18430. <https://doi.org/10.1038/s41598-020-75134-1>.
- (9) Gild, J.; Samiee, M.; Braun, J. L.; Harrington, T.; Vega, H.; Hopkins, P. E.; Vecchio, K.; Luo, J. High-Entropy Fluorite Oxides. *J. Eur. Ceram. Soc.* **2018**, *38*, 3578–3584. <https://doi.org/10.1016/j.jeurceramsoc.2018.04.010>.
- (10) Vinnik, D. A.; Trofimov, E. A.; Zhivulin, V. E.; Zaitseva, O. V.; Gudkova, S. A.; Starikov, A. Yu.; Zherebtsov, D. A.; Kirsanova, A. A.; Häßner, M.; Niewa, R. High-Entropy Oxide Phases with Magnetoplumbite Structure. *Ceram. Int.* **2019**, *45*, 12942–12948. <https://doi.org/10.1016/j.ceramint.2019.03.221>.
- (11) Kirsch, A.; Bøjesen, E. D.; Lefeld, N.; Larsen, R.; Mathiesen, J. K.; Skjærvø, S. L.; Pittkowski, R. K.; Sheptyakov, D.; Jensen, K. M. Ø. High-Entropy Oxides in the Mullite-Type Structure. *Chem. Mater.* **2023**, *35*, 8664–8674. <https://doi.org/10.1021/acs.chemmater.3c01830>.
- (12) Jiang, S.; Hu, T.; Gild, J.; Zhou, N.; Nie, J.; Qin, M.; Harrington, T.; Vecchio, K.; Luo, J. A New Class of High-Entropy Perovskite Oxides. *Scr. Mater.* **2018**, *142*, 116–120. <https://doi.org/10.1016/j.scriptamat.2017.08.040>.

- (13) Li, F.; Zhou, L.; Liu, J.-X.; Liang, Y.; Zhang, G.-J. High-Entropy Pyrochlores with Low Thermal Conductivity for Thermal Barrier Coating Materials. *J. Adv. Ceram.* **2019**, *8*, 576–582. <https://doi.org/10.1007/s40145-019-0342-4>.
- (14) Jiang, B.; Bridges, C. A.; Unocic, R. R.; Pitike, K. C.; Cooper, V. R.; Zhang, Y.; Lin, D.-Y.; Page, K. Probing the Local Site Disorder and Distortion in Pyrochlore High-Entropy Oxides. *J. Am. Chem. Soc.* **2021**, *143*, 4193–4204. <https://doi.org/10.1021/jacs.0c10739>.
- (15) Dąbrowa, J.; Adamczyk, J.; Stępień, A.; Zajusz, M.; Bar, K.; Berent, K.; Świerczek, K. Synthesis and Properties of the Gallium-Containing Ruddlesden-Popper Oxides with High-Entropy B-Site Arrangement. *Materials* **2022**, *15*, 6500. <https://doi.org/10.3390/ma15186500>.
- (16) Johnstone, G. H. J.; González-Rivas, M. U.; Taddei, K. M.; Sutarto, R.; Sawatzky, G. A.; Green, R. J.; Oudah, M.; Hallas, A. M. Entropy Engineering and Tunable Magnetic Order in the Spinel High-Entropy Oxide. *J. Am. Chem. Soc.* **2022**, *144*, 20590–20600. <https://doi.org/10.1021/jacs.2c06768>.
- (17) Witte, R.; Sarkar, A.; Kruk, R.; Eggert, B.; Brand, R. A.; Wende, H.; Hahn, H. High-Entropy Oxides: An Emerging Prospect for Magnetic Rare-Earth Transition Metal Perovskites. *Phys. Rev. Mater.* **2019**, *3*, 034406. <https://doi.org/10.1103/PhysRevMaterials.3.034406>.
- (18) Yin, Y.; Shi, F.; Liu, G.-Q.; Tan, X.; Jiang, J.; Tiwari, A.; Li, B. Spin-Glass Behavior and Magnetocaloric Properties of High-Entropy Perovskite Oxides. *Appl. Phys. Lett.* **2022**, *120*, 082404. <https://doi.org/10.1063/5.0081688>.
- (19) Yu, Y.; Liu, S.; Wang, H.; Zhang, S.; Wang, N.; Jiang, W.; Liu, C.; Ding, W.; Zhang, Z.; Dong, C. Synthesis and Optoelectrical Properties of $\text{Ti}_8\text{Sn}_8\text{Nb}_8\text{Ta}_8\text{Me}_{16}\text{O}_{96}$ (Me=Ga, Fe) Rutile Structure High Entropy Oxides. *Vacuum* **2022**, *203*, 111315. <https://doi.org/10.1016/j.vacuum.2022.111315>.
- (20) Baral, R.; Fierro, H. S.; Rueda, C.; Sahu, B.; Strydom, A. M.; Poudel, N.; Gofryk, K.; Manciu, F. S.; Ritter, C.; Heitmann, T. W.; Belbase, B. P.; Bati, S.; Ghimire, M. P.; Nair, H. S. Signatures of Low-Dimensional Magnetism and Short-Range Magnetic Order in Co-Based Trirutiles. *Phys. Rev. B* **2019**, *100*, 184407. <https://doi.org/10.1103/PhysRevB.100.184407>.
- (21) Rodríguez-Carvajal, J. Recent Advances in Magnetic Structure Determination by Neutron Powder Diffraction. *Physica B* **1993**, *192*, 55–69. [https://doi.org/10.1016/0921-4526\(93\)90108-I](https://doi.org/10.1016/0921-4526(93)90108-I).
- (22) Reimers, J. N.; Greedan, J. E.; Stager, C. V.; Kremer, R. Crystal Structure and Magnetism in CoSb_2O_6 and CoTa_2O_6 . *J. Solid State Chem.* **1989**, *83*, 20–30. [https://doi.org/10.1016/0022-4596\(89\)90049-2](https://doi.org/10.1016/0022-4596(89)90049-2).
- (23) Biesinger, M. C.; Payne, B. P.; Grosvenor, A. P.; Lau, L. W. M.; Gerson, A. R.; Smart, R. St. C. Resolving Surface Chemical States in XPS Analysis of First Row Transition Metals, Oxides and Hydroxides: Cr, Mn, Fe, Co and Ni. *Appl. Surf. Sci.* **2011**, *257*, 2717–2730. <https://doi.org/10.1016/j.apsusc.2010.10.051>.
- (24) Yamashita, T.; Hayes, P. Analysis of XPS Spectra of Fe^{2+} and Fe^{3+} Ions in Oxide Materials. *Appl. Surf. Sci.* **2008**, *254*, 2441–2449. <https://doi.org/10.1016/j.apsusc.2007.09.063>.
- (25) Biesinger, M. C.; Lau, L. W. M.; Gerson, A. R.; Smart, R. St. C. Resolving Surface Chemical States in XPS Analysis of First Row Transition Metals, Oxides and Hydroxides: Sc, Ti, V, Cu and Zn. *Appl. Surf. Sci.* **2010**, *257*, 887–898. <https://doi.org/10.1016/j.apsusc.2010.07.086>.

Supporting Information

Absence of Long-Range Magnetic Ordering in a Trirutile High-Entropy Oxide



Gina Angelo,^a Liana Klivansky,^b Jian Zhang,^b Xin Gui^{a}*

^a Department of Chemistry, University of Pittsburgh, Pittsburgh, PA, 15260, USA

^b The Molecular Foundry, Lawrence Berkeley National Laboratory, Berkeley, CA, 94720, USA

Table of Contents

<u>Table S1</u>	2
<u>Table S2</u>	2
<u>Figure S1</u>	3
<u>Figure S2</u>	4
<u>Figure S3</u>	5
<u>Figure S4</u>	6
<u>Figure S5</u>	7
<u>Molecular Orbital Calculations Details</u>	8
<u>Reference</u>	8

Table S1. The atomic sites of $(\text{Mn}_{0.2}\text{Fe}_{0.2}\text{Co}_{0.2}\text{Ni}_{0.2}\text{Cu}_{0.2})\text{Ta}_2\text{O}_6$ were determined via Rietveld refinement. $(\text{Mn}_{0.2}\text{Fe}_{0.2}\text{Co}_{0.2}\text{Ni}_{0.2}\text{Cu}_{0.2})\text{Ta}_2\text{O}_6$ is in space group $P4_2/mnm$ (no. 136) with parameters $a = 4.73483$ (3) Å and $c = 9.19965$ (5) Å. M stands for 3d transition metals.

	<i>x</i>	<i>y</i>	<i>z</i>
M1	0	0	0
Ta1	0	0	0.3316 (1)
O1	0.2989 (8)	0.2989 (8)	0
O2	0.2858 (5)	0.2858 (5)	0.3259 (1)

Table S2 EDS results of MTa_2O_6 for three different areas of the sample.

	Spectra	Mn	Fe	Co	Ni	Cu	Ta
Area 1	Spectrum 5	1.83	1.78	1.78	2.78	1.84	18.24
	Spectrum 6	1.99	2.46	2.11	2.08	1.99	19.60
	Spectrum 7	1.82	2.37	2.01	1.89	1.83	18.09
	Spectrum 8	1.87	2.16	1.80	1.95	1.73	17.79
	Average	1.88	2.19	1.93	2.18	1.85	18.43
Area 2	Spectrum 9	1.36	1.55	1.77	4.03	1.25	16.93
	Spectrum 10	1.52	1.75	1.72	2.99	1.18	16.50
	Spectrum 11	1.60	2.27	1.90	3.06	1.02	17.80
	Spectrum 12	1.75	1.74	1.87	3.53	1.37	18.31
	Average	1.56	1.83	1.82	3.40	1.21	17.39
Area 3	Spectrum 13	1.64	2.90	1.82	0.09	1.98	16.76
	Spectrum 14	1.95	3.14	2.02	1.36	2.01	18.81
	Spectrum 15	1.76	2.62	2.28	1.39	1.80	18.48
	Spectrum 16	1.92	2.88	2.18	1.08	2.33	19.53
	Average	1.82	2.89	2.08	0.98	2.03	18.40
	Total Average	1.75	2.30	1.94	2.19	1.69	18.07
	Standard deviation	0.19	0.52	0.18	1.01	0.40	1.00

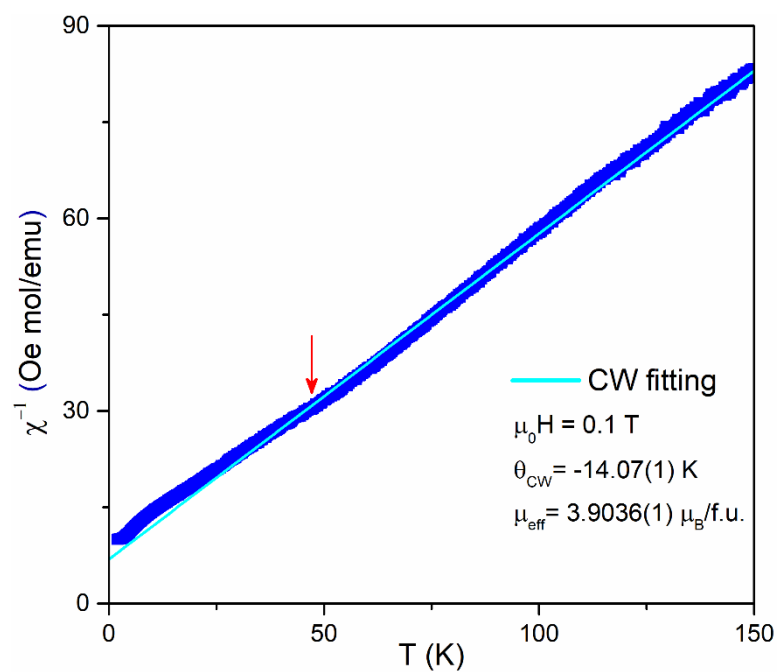


Figure S1. Deviation from the Curie-Weiss (CW) behavior at low temperatures.

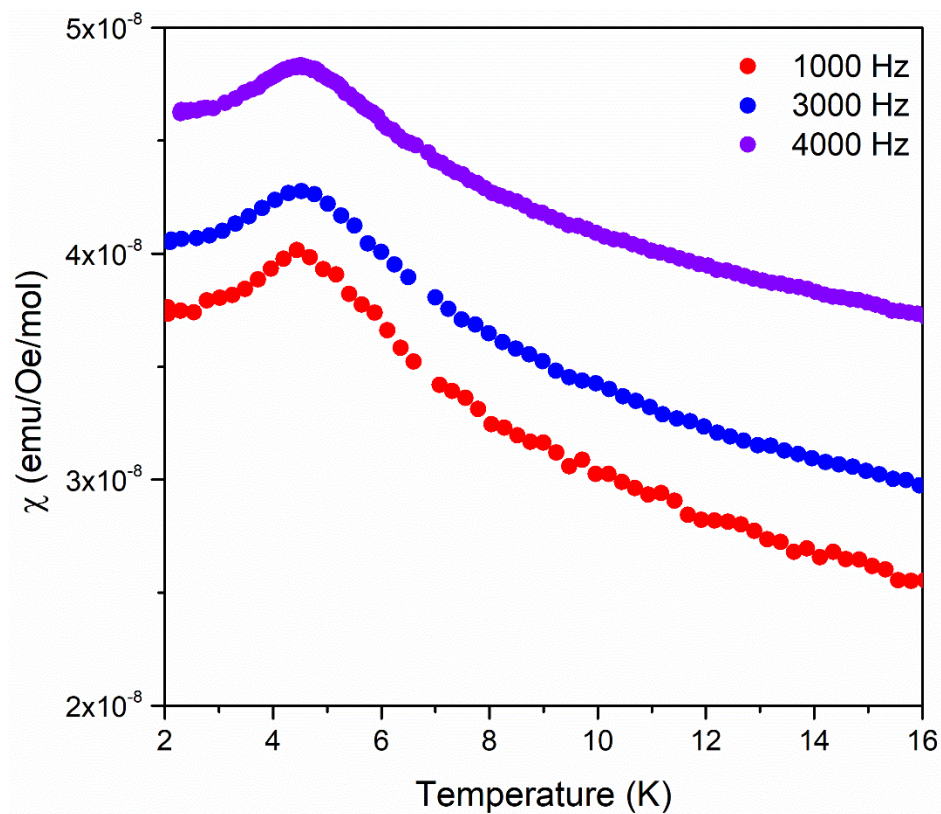


Figure S2. AC magnetic susceptibility of $(\text{Mn}_{0.2}\text{Fe}_{0.2}\text{Co}_{0.2}\text{Ni}_{0.2}\text{Cu}_{0.2})\text{Ta}_2\text{O}_6$ under various frequencies. The applied DC magnetic field is 100 Oe and the AC field is 10 Oe.

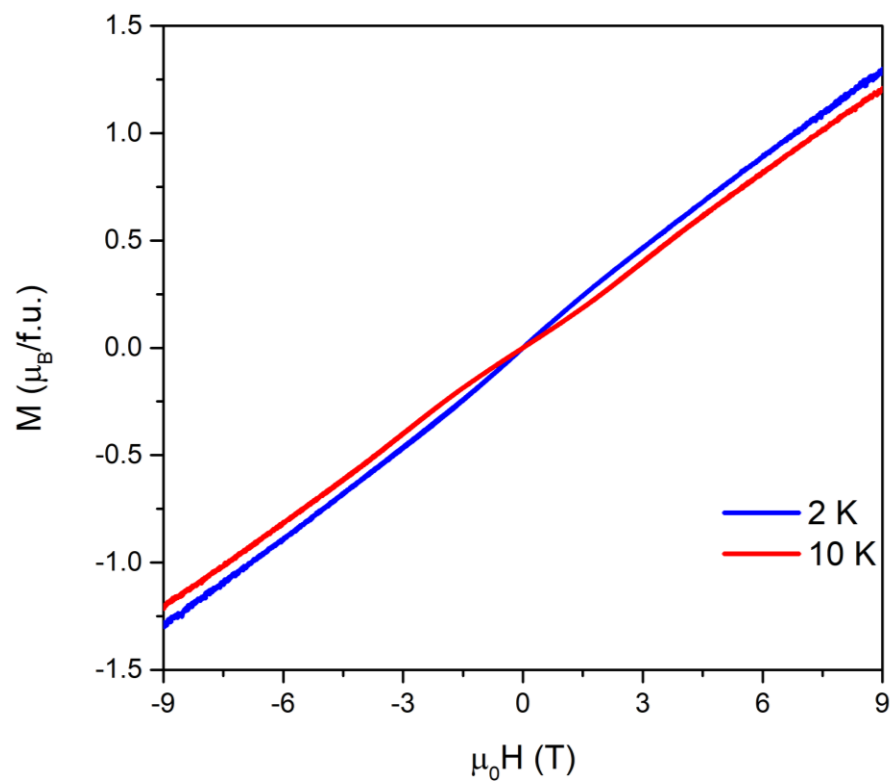


Figure S3. Hysteresis loops of $(\text{Mn}_{0.2}\text{Fe}_{0.2}\text{Co}_{0.2}\text{Ni}_{0.2}\text{Cu}_{0.2})\text{Ta}_2\text{O}_6$ at 2 K (blue) and 10 K (red).

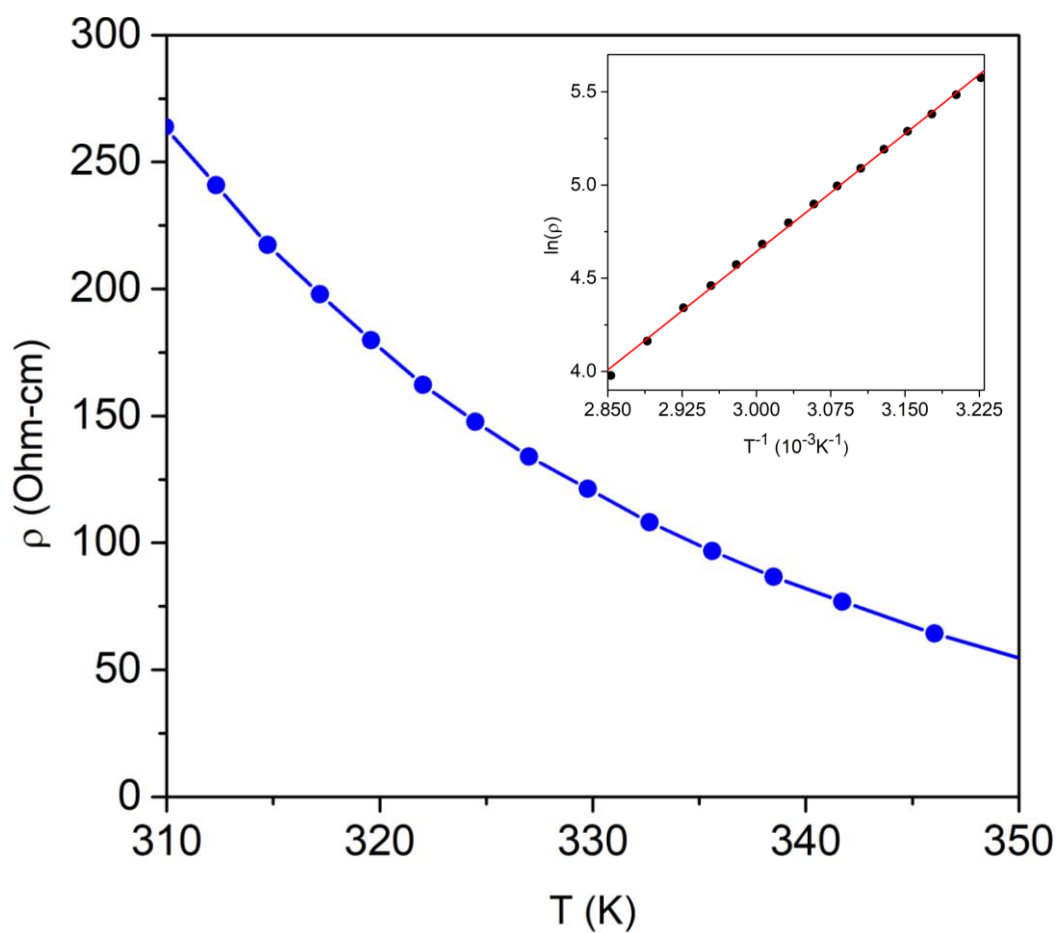


Figure S4. Resistivity of $(\text{Mn}_{0.2}\text{Fe}_{0.2}\text{Co}_{0.2}\text{Ni}_{0.2}\text{Cu}_{0.2})\text{Ta}_2\text{O}_6$ from 310 K to 350K displaying insulating behavior. The inset graph is of the linear relationship between $\ln(\rho)$ and T^{-1} .

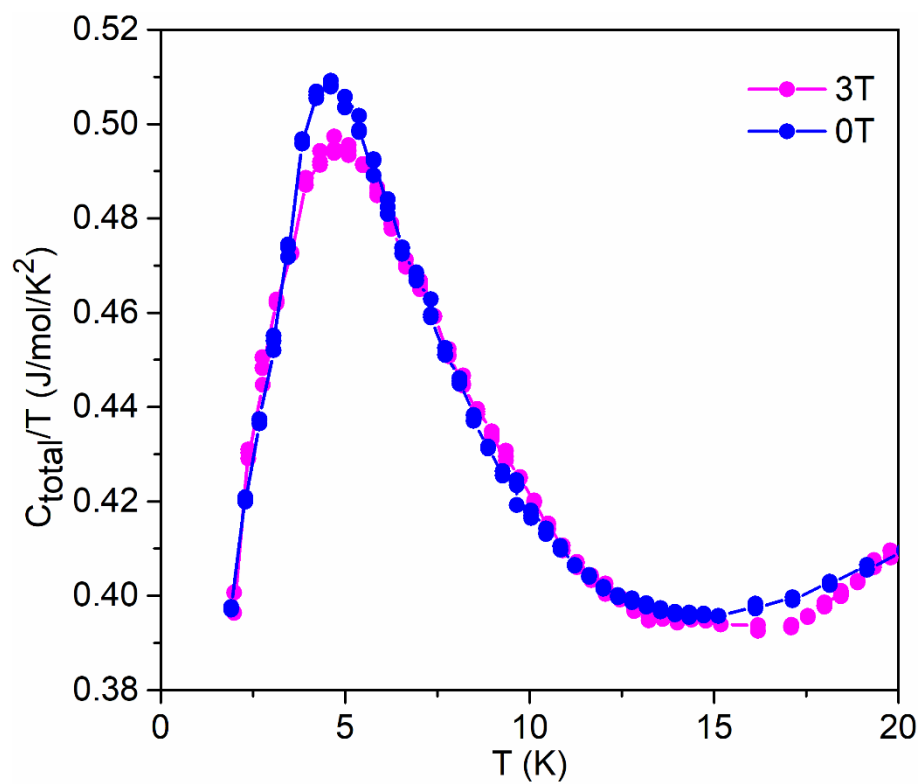


Figure S5. Temperature-dependent heat capacity of $(\text{Mn}_{0.2}\text{Fe}_{0.2}\text{Co}_{0.2}\text{Ni}_{0.2}\text{Cu}_{0.2})\text{Ta}_2\text{O}_6$ measured under magnetic field $\mu_0 H = 0$ T and 3 T.

Molecular Orbital (MO) Calculation: Semi-empirical extended-Hückel-tight-binding (EHTB) methods and CAESAR packages are used in calculating molecular orbitals of the parent compound, CoTa₂O₆.¹ The basis sets for Co are: 4s: Hii = -9.21 eV, $\zeta_1 = 2$, coefficient1 = 1.0000; 4p: Hii = -5.29 eV, $\zeta_1 = 2$, coefficient1 = 1.000; 3d: Hii = -13.18 eV, $\zeta_1 = 5.55$, coefficient1 = 0.568, $\zeta_2 = 2.1$, coefficient2 = 0.606. For Ta: 6s: Hii = -10.1 eV, $\zeta_1 = 2.28$, coefficient1 = 1.000; 6p: Hii = -6.86 eV, $\zeta_1 = 2.241$, coefficient1 = 1.000; 5d: Hii = -12.1 eV, $\zeta_1 = 4.762$, coefficient1 = 0.6815, $\zeta_2 = 1.938$, coefficient2 = 0.5589. For O: 2s: Hii = -32.29999 eV, $\zeta_1 = 2.275$, coefficient1 = 1.000; 2p: Hii = -14.8 eV, $\zeta_1 = 2.275$, coefficient1 = 1.000.

Reference

1. Hoffmann, R. An extended Hückel theory. I. hydrocarbons. *J. Chem. Phys.* **1963**, 39, 1397-1412.